



**HAL**  
open science

## Three-dimensional foam flow resolved by fast X-ray tomographic microscopy

Christophe Raufaste, Benjamin Dollet, Kevin Mader, Stéphane Santucci,  
Rajmund Mokso

► **To cite this version:**

Christophe Raufaste, Benjamin Dollet, Kevin Mader, Stéphane Santucci, Rajmund Mokso. Three-dimensional foam flow resolved by fast X-ray tomographic microscopy. *EPL - Europhysics Letters*, 2015, 111 (3), pp.38004. 10.1209/0295-5075/111/38004 . hal-01192711

**HAL Id: hal-01192711**

**<https://univ-rennes.hal.science/hal-01192711>**

Submitted on 3 Sep 2015

**HAL** is a multi-disciplinary open access archive for the deposit and dissemination of scientific research documents, whether they are published or not. The documents may come from teaching and research institutions in France or abroad, or from public or private research centers.

L'archive ouverte pluridisciplinaire **HAL**, est destinée au dépôt et à la diffusion de documents scientifiques de niveau recherche, publiés ou non, émanant des établissements d'enseignement et de recherche français ou étrangers, des laboratoires publics ou privés.

# Three-dimensional foam flow resolved by fast X-ray tomographic microscopy

C. RAUFASTE<sup>1</sup>, B. DOLLET<sup>2</sup>, K. MADER<sup>3,4</sup>, S. SANTUCCI<sup>5</sup> and R. MOKSO<sup>4</sup>

<sup>1</sup> *Université Nice Sophia Antipolis, CNRS, LPMC, UMR 7336, Parc Valrose, 06100 Nice, France*

<sup>2</sup> *Institut de Physique de Rennes, UMR CNRS 6251, Université de Rennes 1, Campus de Beaulieu, 35042 Rennes Cedex, France*

<sup>3</sup> *Institute for Biomedical Engineering, University and ETH Zurich, Gloriastrasse 35, Zurich, Switzerland*

<sup>4</sup> *Swiss Light Source, Paul Scherrer Institute, Villigen, Switzerland*

<sup>5</sup> *Laboratoire de Physique, ENS Lyon, UMR CNRS 5672, 46 allée d'Italie, 69007 Lyon, France*

PACS 83.80.Iz – Emulsions and foams

**Abstract** – Adapting fast tomographic microscopy, we managed to capture the evolution of the local structure of the bubble network of a 3D foam flowing around a sphere. As for the 2D foam flow around a circular obstacle, we observed an axisymmetric velocity field with a recirculation zone, and indications of a negative wake downstream the obstacle. The bubble deformations, quantified by a shape tensor, are smaller than in 2D, due to a purely 3D feature: the azimuthal bubble shape variation. Moreover, we were able to detect plastic rearrangements, characterized by the neighbor-swapping of four bubbles. Their spatial structure suggests that rearrangements are triggered when films faces get smaller than a characteristic area.

Foam rheology is an active research topic [1–4], motivated by applications in ore flotation, enhanced oil recovery, food or cosmetics [5]. Because foams are opaque, imaging their flow in bulk at the bubble scale is challenging. To bypass this difficulty, 2D flows of foams confined as a bubble monolayer, which structure is easy to visualize, have been studied. However, the friction induced by the confining plates may lead to specific effects [6], irrelevant for bulk rheology. In 3D, diffusive-wave spectroscopy has been used to detect plastic rearrangements [7, 8]. These events, called T1s, characterized in 2D by the neighbor swapping of four bubbles in contact, are of key importance for flow rheology, since their combination leads to the plastic flow of foams. Magnetic resonance imaging has also been used to measure the velocity field in 3D [9]. However, both these techniques resolve neither the bubble shape, nor the network of liquid channels (Plateau borders, PBs) within a foam. In contrast, X-ray tomography renders well its local structure. However, the long acquisition time of a tomogram, over a minute until very recently, constituted its main limitation, allowing to study only slow coarsening processes [10, 11].

Here, we report the first quantitative study of a 3D foam flow around an obstacle. Such challenge was tackled

thanks to a dedicated ultra fast and high resolution imaging set-up, recently developed at the TOMCAT beam line of the Swiss Light Source [12]. High resolution tomogram covering a volume of  $4.8 \times 4.8 \times 5.6 \text{ mm}^3$  with a voxel edge length of  $5.3 \mu\text{m}$  could be acquired in around 0.5 s, allowing to follow the evolving structure of the bubbles and PB network. Our image analysis shows that the 3D foam flow around a sphere is qualitatively similar to the 2D flow around a circular obstacle: we reveal an axisymmetric velocity field, with a recirculation zone around the sphere in the frame of the foam, and a negative wake downstream the obstacle. Bubble deformations are smaller (in the diametral plane along the mean direction of the flow  $z$ ) than for a 2D flow, thanks to the extra degree of freedom allowing an azimuthal deformation: bubbles appear oblate before, and prolate after, the obstacle. Finally, we were able to detect plastic rearrangements, characterized by the neighbor-swapping of four bubbles and the exchange of two four-sided faces. Our observations suggest that those events are triggered when the bubble faces get smaller than a characteristic size around  $R_c^2$ , given by a cutoff length of the PB  $R_c \simeq 130 \mu\text{m}$  in the case of our foam.

*Experimental set-up* – We prepared a foaming solution following the protocol of [13]: we mixed 6.6% of sodium

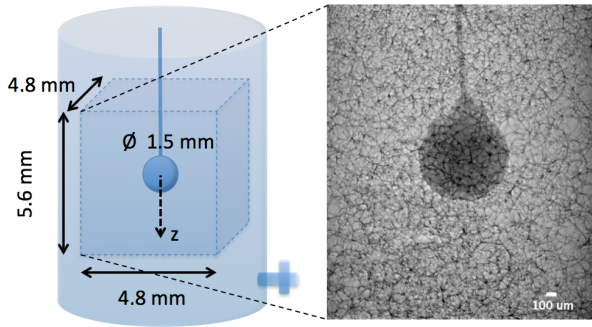


Fig. 1: A plastic bead of 1.5 mm diameter glued to a capillary is placed in the middle of the cylindric chamber of 22 mm diameter and 50 mm height. The acquired tomograms cover the central region with a volume of  $4.8 \times 4.8 \times 5.6 \text{ mm}^3$ . A typical X-ray projection image is shown on the right.

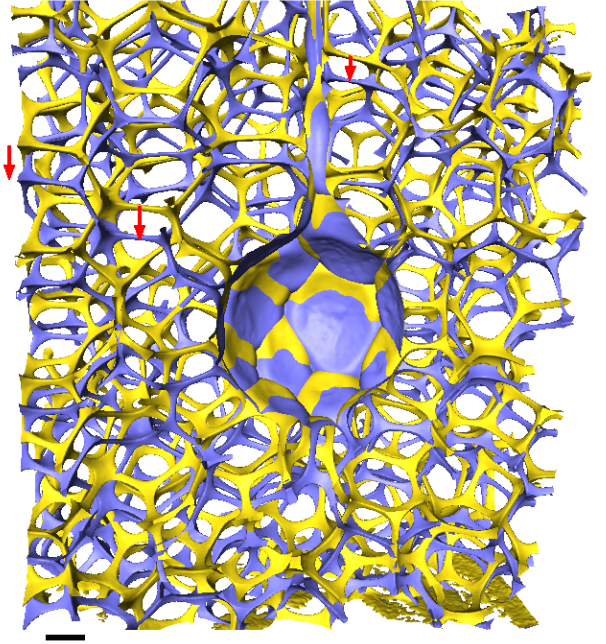


Fig. 2: 3D volume representation of two instances in the foam flow. The PBs and vertices are colored in yellow and blue for time steps  $t_0$  and  $t_0 + 35 \text{ s}$  respectively. The scale bar is  $300 \mu\text{m}$ . Red arrows indicate the flow direction.

49 lauryl ether sulfate (SLES) and 3.4% of cocamidopropyl  
 50 betaine (CAPB) in mass in ultrapure water; we then dis-  
 51 solved 0.4% in mass of myristic acid (MAc), by stirring and  
 52 heating at  $60^\circ\text{C}$  for one hour, and we diluted 20 times this  
 53 solution. A few mL of solution was poured in the bottom of  
 54 a cylindrical perspex chamber of diameter 22 mm and  
 55 height 50 mm. Bubbling air through a needle immersed in  
 56 this solution, a foam was created until it reached the top  
 57 of the chamber. The bottom of the cell contains a tube  
 58 connected to the open air and closed by a tap. Controlling  
 59 the opening of the tap, we could obtain a slow steady flow  
 60 of the liquid foam. Its mean velocity determined a poste-  
 61 riori by image analysis is equal to  $v_{\text{flow}} = 8 \mu\text{m/s}$ . While  
 62 flowing, the foam is deformed due to the presence of an  
 63 obstacle, a smooth plastic bead of diameter  $2a = 1.5 \text{ mm}$ ,  
 64 attached to a capillary to fix its position in the middle of  
 65 the chamber (Fig. 1). Because the cell makes a full rota-  
 66 tion in 0.5 s, the foam experiences centrifugal acceleration,  
 67 but it remains below  $0.5 \text{ m/s}^2$  within the observation win-  
 68 dow, hence negligible compared to gravity.

69 The experiments were performed at the TOMCAT  
 70 beamline of the Swiss Light Source. Filtered polychro-  
 71 matic X-rays with mean energy of 30 keV were incident  
 72 on a custom made flow cell (Fig. 1) attached to the to-  
 73 mography stage with three translational and a rotational  
 74 degrees of freedom. The X-rays passing through the foam  
 75 in the chamber were converted to visible light by a  $100 \mu\text{m}$   
 76 thick LuAG:Ce and detected by a 12 bit CMOS camera.  
 77 Typically 550 radiographic projections acquired with 1 ms  
 78 exposure time at equidistant angular positions of the sam-  
 79 ple were reconstructed into a 3D volume of  $4.8 \times 4.8 \times 5.6$   
 80  $\text{mm}^3$  with isotropic voxel edge length of  $ps = 5.3 \mu\text{m}$ .  
 81 Such a 3D snapshot of the flowing foam is acquired in  
 82  $t_{\text{scan}} = 0.55 \text{ s}$ , ensuring that motion artifacts are absent  
 83 since  $t_{\text{scan}} < ps/v_{\text{flow}}$ . In order to follow the structural  
 84 changes of the foam during its flow around the obstacle,  
 85 we recorded a tomogram every 35 seconds for approxi-  
 86 mately 20 minutes (resulting in around 36 tomograms).  
 87 The tomograms quality is enhanced using not only the X-  
 88 rays attenuation by the sample, but also the phase shift

of the partially coherent X-ray beam as it interacts with  
 the foaming solution in the PBs and senses the electron  
 density variation in the sample [12]. This phase shift was  
 retrieved using a single phase object approximation [14].

*Image analysis* – The tomograms are then segmented,  
 separating the PBs and vertices from air. Fig. 2 shows  
 two successive time steps of the 3D snapshots of the re-  
 constructed PBs network during the foam flow around  
 the sphere. We measured the liquid fraction from the  
 segmented images, by computing the relative surface occu-  
 pied by the PBs and vertices on individual horizontal  
 slices. We measured an averaged liquid fraction of 4% over  
 a tomogram, which did not evolve significantly during our  
 experiments.

Then, we reconstructed and identified individual bub-  
 bles of the flowing foam, following the procedure we re-  
 cently developed and validated on static foam samples,  
 imaged at the same acquisition rate and spatial resolu-  
 tion [15]. We did not observe any evolution of the size  
 distribution of the polydisperse foam studied here, with  
 an average volume  $V = 0.36 \pm 0.13 \text{ mm}^3$ , hence coarsen-  
 ing remains negligible. Typically, 160 bubbles are tracked  
 between two successive 3D snapshots, leading to statistics  
 over 5600 bubbles. Bubbles smaller than  $0.01 \text{ mm}^3$  cannot  
 be discriminated from labeling artifacts [15], and thus, are  
 discarded.

*Velocity field* – From the bubble tracking, we could mea-  
 sure their velocity  $\vec{V}$  around the obstacle. Statistics are  
 performed in the diametral ( $\rho z$ ) plane of the cylindrical co-  
 ordinates ( $\rho\phi z$ ). We have checked that our results do not

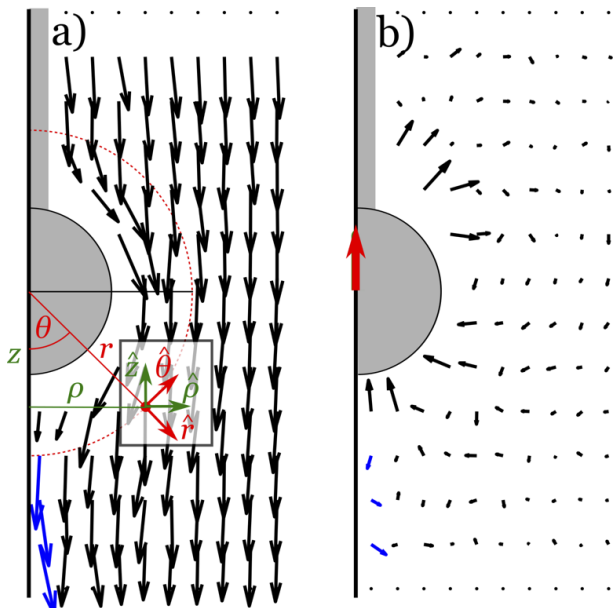


Fig. 3: Velocity fields in the  $(\rho z)$  plane, (a) in the lab frame. Both the  $(\rho z)$  or the  $(r\theta)$  polar coordinates can be used. The unit vectors  $(\hat{\rho}, \hat{z})$  or  $(\hat{r}, \hat{\theta})$  are plotted for  $r = 1.5$  mm in the plane. The normalized velocity field obtained by subtracting the mean flow velocity is shown in (b). The gray half-disc represents the obstacle (diameter 1.5 mm). The red arrow centered on the semi-obstacle gives the velocity scale of  $8 \mu\text{m/s}$ . Blue arrows show the negative wake effect.

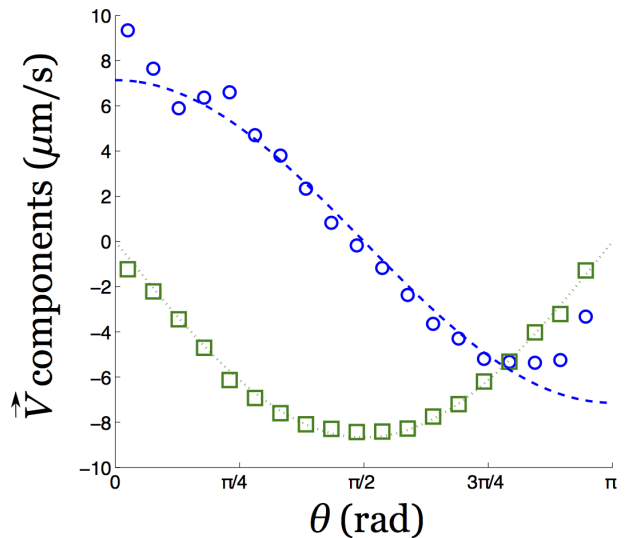


Fig. 4: Velocity components measured at a distance  $r = 1.5$  mm from the obstacle center as a function of the polar angle  $\theta$ :  $V_r$  (blue circles) and  $V_\theta$  (green squares) in the  $(r\theta)$  frame. The lines hold for a potential flow model.

depend significantly on the angular coordinate  $\phi$  (see also below), and we have averaged over this coordinate, as well as over time, thanks to the steadiness of the flow. The diametral plane is meshed into rectangular boxes ( $0.25 \times 0.40 \text{ mm}^2$ ). Consistently with the angular averaging procedure, we have checked that the number of bubbles analyzed per box is roughly proportional to the distance of the box to the symmetry axis (data not shown). Averages are weighted by the bubble volumes.

The velocity field is plotted in Fig. 3. In average over all patches, the  $\phi$ -component of the averaged velocity vector is 50 times smaller than its  $\rho z$ -component, hence the flow is axisymmetric. As expected, the velocity is uniform far from the obstacle, its amplitude decreases close to the leading and trailing points of the sphere, and increases along its sides. Accordingly, there is a clear recirculation zone surrounding the obstacle in the frame of the flowing foam (Fig. 3b). It is worth noting that, compared to 2D foam flows around a circular obstacle [16–19], the range of influence of the obstacle on the flow field is smaller.

Interestingly, there is a zone downstream the obstacle and close to the symmetry axis where the streamwise velocity component is larger than the mean velocity or, equivalently, where the velocity opposes that of the obstacle in the frame of the flowing foam. This reminds the so-called *negative wake*, revealed in viscoelastic fluids [20–22] and also evidenced in 2D foams [17]. However, a difficulty intrinsic to the 3D axisymmetric geometry is

that the statistics is poor in these boxes close to the symmetry axis (about 10 bubbles per box over the full run), and should be improved in the future. The strong fore-aft asymmetry of the flow evidenced by this negative wake confirms that the foam cannot be modelled as a viscoplastic fluid, which gives a fore-aft-symmetric flow [23]: it is intrinsically viscoelastoplastic.

To further quantify the velocity field, its components  $V_r$  and  $V_\theta$  at a distance  $r = 1.5$  mm (one obstacle diameter) from the obstacle center are plotted as a function of  $\theta$  in Fig. 4. We have checked that choosing another distance (e.g.  $r = 2$  mm) does not change the qualitative features of the velocity field. The component  $V_\theta$  is negative, because  $\theta$  is directed upstream.  $|V_\theta|$  is maximum at  $\theta = \pi/2$ , and  $V_\theta$  is almost fore-aft symmetric (i.e. symmetric with respect to the axis  $\theta = \pi/2$ ). The component  $V_r$  is positive for  $\theta < \pi/2$ , and negative for  $\theta > \pi/2$ . Contrary to  $V_\theta$ ,  $V_r$  is fore-aft asymmetric. The absolute value of  $V_r$  monotonously grows on both sides away from  $\pi/2$  (albeit with noise near 0), it reaches a local extremum near  $3\pi/4$  then decreases as  $\theta$  increases towards  $\pi$ . To further reveal this asymmetry, a comparison is made with a potential flow model, which velocity field writes [24]:  $V_r = U(1 - r^3/a^3) \cos \theta$ , and  $V_\theta = -U(1 + r^3/2a^3) \sin \theta$ , where  $U$  is the uniform velocity far from a spherical obstacle of diameter  $2a$ . We proceed as follows: first, we fit  $V_\theta$  with  $U$  as the sole free fitting parameter. This procedure gives the dotted line on Fig. 4, with  $U = 8.2 \mu\text{m/s}$ . We then use this value of  $U$  in the potential flow formula for  $V_r$ , and we plot it as a dashed line in Fig. 4. While  $V_\theta$  is very similar to the potential flow case (which is expected, since this only tests its fore-aft symmetry),  $V_r$  exhibits deviations from potential flow close to  $\theta = 0$  and  $\pi$ . In particular,  $V_r$  reaches a value significantly larger than  $U$



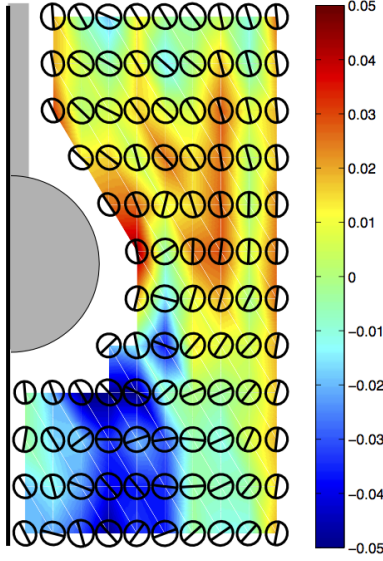


Fig. 5: Projection of the bubble deformation field in the  $(\rho z)$  plane. Ellipses of bubbles are dilated by a factor of 0.5. The colormap gives the amplitude of the normalized deformation in the azimuthal direction.

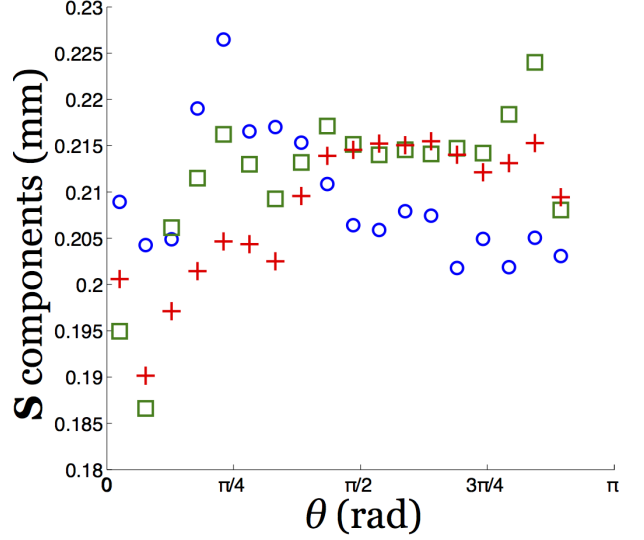


Fig. 6: Shape components measured at a distance  $r = 1.5$  mm from the obstacle center as a function of the polar angle  $\theta$ :  $S_{rr}$  (blue circles),  $S_{\theta\theta}$  (green squares) and  $S_{\phi\phi}$  (red crosses) in the  $(r\theta\phi)$  frame. The  $S_{r\theta}$  component is approximately 100 times smaller than the other components and is not displayed.

181 close to  $\theta = 0$ , which is a signature of the negative wake.  
182 The deviation close to  $\theta = \pi$  is more difficult to interpret,  
183 and might be due to the presence of the capillary holding  
184 the obstacle

185 *Bubble deformation* – Given the set of coordinates  $\{\mathbf{r}\}$   
186 of the voxels inside a bubble, we define its inertia ten-  
187 sor  $\mathbf{I} = \langle (\mathbf{r} - \langle \mathbf{r} \rangle) \otimes (\mathbf{r} - \langle \mathbf{r} \rangle) \rangle$ , and its shape tensor as  
188  $\mathbf{S} = \mathbf{I}^{1/2}$ . This operation is valid because  $\mathbf{I}$  (and hence  
189  $\mathbf{S}$ ) is a symmetric and definite tensor. Alike the velocity  
190 field, averages are performed inside boxes to obtained a  
191 shape field (Fig. 5). The bubble deformation is quan-  
192 tified by the eigenvectors/values of the shape tensor. In  
193 good approximation, two of them ( $S_{\rho z}^+$  and  $S_{\rho z}^-$ ) are found  
194 inside the  $(\rho z)$  plane, the other corresponds to the pro-  
195 jection of the tensor along the azimuthal direction ( $S_{\phi\phi}$ ).  
196 An effective radius is defined by  $R_{\text{eff}} = (S_{\rho z}^+ S_{\rho z}^- S_{\phi\phi})^{1/3}$ .  
197 The bubbles deformation in the  $(\rho z)$  plane is represented  
198 by ellipses of semi-axes  $S_{\rho z}^+$  and  $S_{\rho z}^-$ . The direction of the  
199 largest one,  $S_{\rho z}^+$ , is emphasized by a line across the el-  
200 lipse (Fig. 5). Deformation in the azimuthal direction is  
201 quantified by  $(S_{\phi\phi} - R_{\text{eff}})/R_{\text{eff}}$  in colormap. The orienta-  
202 tion of the ellipses in the  $(\rho z)$  plane exhibits a clear trend  
203 comparable to the 2D case [17, 25]. They are elongated  
204 streamwise on the obstacle side and at the trailing edge.  
205 In between, the ellipses rotate  $180^\circ$  to connect these two  
206 regions. We noticed that the deformation of the bubbles is  
207 much smaller than for a 2D foam with the same liquid frac-  
208 tion [17, 25]. The deformation in the azimuthal direction  
209 exhibits dilation/compression up to 5% only. The quan-  
210 tity  $(S_{\phi\phi} - R_{\text{eff}})/R_{\text{eff}}$  is positive upstream (oblate shape)  
211 to favor the passage around the obstacle (Fig. 5). The  
212 third dimension tends therefore to reduce the bubble de-  
213 formation in the  $(\rho z)$  plane by increasing the deformation  
214 in the azimuthal direction. This effect is opposite down-

stream, right after the obstacle, where the bubbles are  
215 prolate. 216

217 These features are further quantified by plotting the  
218 normal components of the shape tensor  $S_{rr}$ ,  $S_{\theta\theta}$  and  $S_{\phi\phi}$   
219 as a function of  $\theta$  at  $r = 1.5$  mm, in Fig. 6. This graph  
220 shows that these normal components remain within a nar-  
221 row range, between 0.19 mm and 0.22 mm, confirming  
222 that the bubbles are weakly deformed. These values cor-  
223 respond to the typical bubble size. For  $\theta > \pi/2$  (i.e. up-  
224 stream the obstacle),  $S_{rr}$  is lower than  $S_{\theta\theta}$  and  $S_{\phi\phi}$ , which  
225 are approximately equal: hence, the bubbles are squashed  
226 against the obstacle. Conversely, for  $\theta < 1.2$  rad,  $S_{rr}$  is  
227 larger than  $S_{\theta\theta}$  and  $S_{\phi\phi}$ : the bubbles are stretched away  
228 from the obstacle. Hence, close to the axis  $\theta = 0$ , the bub-  
229 bles are elongated streamwise more than spanwise. The  
230 origin of the negative wake then becomes clear: by elas-  
231 tically relaxing this deformation, the bubbles “push” the  
232 streamlines away from the axis  $\theta = 0$ . Hence, the velocity  
233 has to decrease towards its limiting value  $U$  as the bubbles  
234 are advected away from the obstacle.

235 *Plastic rearrangements* – Automated tracking of bub-  
236 ble rearrangements was hindered by the high sensitivity  
237 of such procedure to small defects in the reconstruction  
238 of the bubble topology. Description of the contact be-  
239 tween bubbles requires to rebuild precisely the faces be-  
240 tween bubbles, which would require a finer analysis [26].  
241 Nevertheless, we managed to detect manually four individ-  
242 ual events, corresponding to the rearrangements of neigh-  
243 boring bubbles. We provide below a detailed descrip-  
244 tion of one typical example (Fig. 7); the features of the  
245 three other ones were found to be the same. Those rear-  
246 rangements consist of the swapping of four neighboring  
247 bubbles, with an exchange of four-sided faces, called T1s

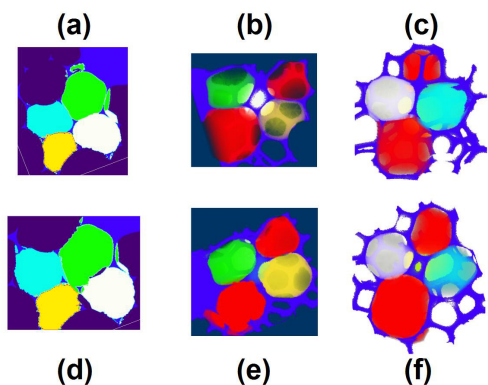


Fig. 7: Example of a T1 in 3D. The white and cyan bubbles lose contact, whereas the green and yellow bubbles come into contact. The red bubbles are the two bubbles that are in contact with these four bubbles over the rearrangement. Three different projections are shown: across the four bubbles that swap neighbors, (a) before and (d) after the T1; (b) in the plane of the face that is about to disappear, and (e) in this plane after the T1; (c) in the plane of the face that is about to appear and (f) in this plane after the T1.

or quadrilateral-quadrilateral (QQ) transitions by Reinelt and Kraynik [27,28]. We did not observe three-sided faces during a T1 as reported by [29]. These are likely highly unstable, transient states which are too short-lived to be captured by tomography. The QQ transitions observed involve two bubbles losing one face and two bubbles gaining one face. As can be seen on the projection plane across these four bubbles (Fig. 7a and d), this is analogous to T1s in 2D, which always involve four bubbles, two losing one side and two gaining one side. The distance between the two bubbles coming into contact decreases of  $150 \mu\text{m}$ , from  $1.10 \text{ mm}$  before the T1 to  $0.95 \text{ mm}$  after, while the distance between the two bubbles losing contact increases of  $200 \mu\text{m}$ , from  $1.03 \text{ mm}$  before the T1 to  $1.23 \text{ mm}$  after. We checked that the distances between the other bubbles around this T1 change much less. This corroborates the vision of a T1 quite similar as in 2D, acting as a quadrupole in displacement, with most effect on the bubbles in the plane. On the other hand, the variation of shape anisotropy of the bubbles involved in the T1 did not show significant trends.

We went further on in the characterization of the spatial structure of those rearrangements. Bubble faces comprise a thin film surrounded by a thick network of PBs and vertices. We have observed that the thin film part is usually very small for faces that are about to disappear, or that have just appeared, during a rearrangement. However, due to the finite radius of the PBs and of the finite size of the vertices, the “skeleton” of these faces is not arbitrarily small. Quantitatively, we measured on the images a PB radius  $R_c = 130 \mu\text{m}$ . We also measured the area of the skeleton of the faces on 2D projections along the plane of the faces (we did not observe significantly non-planar faces). We always found skeleton areas larger than

$3.4 \times 10^4 \mu\text{m}^2$ , which is of the order of  $R_c^2$ . This suggests an interesting analogy with the cut-off edge length in 2D foams expected in theory [30,31], and measured in both simulations [32] and experiments [16]. In 2D foams and emulsions, when the distance between two approaching vertices reaches a certain length, a rearrangement occurs. This happens usually when the two PBs decorating the two neighboring vertices start to merge; hence, the order of magnitude of the cut-off length is  $R_c$ . For 3D foams, our observations suggest that there is a cut-off *area* of the order of  $R_c^2$  below which a face becomes unstable, triggering a rearrangement.

In summary, we have provided the first experimental measurement of a 3D time- and space-resolved foam flow measured directly from individual bubble tracking, with novel results on all the essential features of liquid foam mechanics: elasticity, plasticity and flow, through descriptions of shape field, T1 events, and velocity field. Such experimental results could be achieved thanks to the recent advances of both high resolution and fast X-ray tomography and quantitative analysis tools. We discovered differences between 2D and 3D flows in that the range of influence of the obstacle on the flow field is smaller in the 3D case. The same is true for the deformation of the bubbles which is much smaller in the 3D case. Perspectives include further refinements of the analysis tools [15,26], to fully automatize the detection of rearrangements, to increase statistics and to study various geometries. Imaging the 3D flow at the bubble scale may shed new light on pending issues on shear localization [9] and nonlocal rheology [33].

\* \* \*

We thank Gordan Mikuljan from SLS who realized the experimental cells, Marco Stampanoni for supporting this project, the GDR 2983 Mousses et Émulsions (CNRS) for supporting travel expenses, François Graner, Gilberto L. Thomas and Jérôme Lambert for discussions and the Paul Scherrer Institute for granting beam time to perform the experiments.

## REFERENCES

- [1] WEAIRE D. and HUTZLER S., *The Physics of Foams* (Oxford University Press) 1999.
- [2] CANTAT I., COHEN-ADDAD S., ELIAS F., GRANER F., HÖHLER R., PITOIS O., ROUYER F. and SAINT-JALMES A., *Foams, Structure and Dynamics* (Oxford University Press) 2013.
- [3] COHEN-ADDAD S. and HÖHLER R. and PITOIS O., *Annu. Rev. Fluid Mech.*, **45** (2013) 241.
- [4] DOLLET B. and RAUFASTE C., *C. R. Physique*, **15** (2014) 731.
- [5] STEVENSON P., *Foam Engineering: Fundamentals and Applications* (Wiley) 2012.
- [6] WANG Y., KRISHAN K. and DENNIN M., *Phys. Rev. E*, **73** (2006) 031401.

- 335 [7] DURIAN D. J., WEITZ D. A. and PINE D. J., *Science*,  
336 **252** (1991) 686.
- 337 [8] COHEN-ADDAD S. and HÖHLER R., *Phys. Rev. Lett.*, **86**  
338 (2001) 4700.
- 339 [9] OVARLEZ G., KRISHAN K. and COHEN-ADDAD S., *Euro-*  
340 *phys. Lett.*, **91** (2010) 68005.
- 341 [10] LAMBERT J., CANTAT I., DELANNAY R., MOKSO R.,  
342 CLOETENS P., GLAZIER J. A. and GRANER F., *Phys.*  
343 *Rev. Lett.*, **99** (2007) 058304.
- 344 [11] LAMBERT J., MOKSO R., CANTAT I., CLOETENS P.,  
345 GLAZIER J. A., GRANER F. and DELANNAY R., *Phys.*  
346 *Rev. Lett.*, **104** (2010) 248304.
- 347 [12] MOKSO R., MARONE F. and STAMPANONI M., *AIP Conf.*  
348 *Proc.*, **1234** (2010) 87.
- 349 [13] GOLEMANOV K., DENKOV N. D., TCHOLAKOVA S.,  
350 VETHAMUTHU M. and LIPS A., *Langmuir*, **24** (2008)  
351 9956.
- 352 [14] PAGANIN D., MAYO S. C., GUREYEV T. E., MILLER P.  
353 R. and WILKINS S. W., *J. Microsc.*, **206** (2002) 33.
- 354 [15] MADER K., MOKSO R., RAUFASTE C., DOLLET B., SAN-  
355 TUCCI S., LAMBERT J. and STAMPANONI M., *Colloids*  
356 *Surf. A*, **415** (2012) 230.
- 357 [16] RAUFASTE C., DOLLET B., COX S., JIANG Y. and  
358 GRANER F., *Eur. Phys. J. E*, **23** (2007) 217.
- 359 [17] DOLLET B. and GRANER F., *J. Fluid Mech.*, **585** (2007)  
360 181.
- 361 [18] MARMOTTANT P., RAUFASTE C. and GRANER F., *Eur.*  
362 *Phys. J. E*, **25** (2008) 371.
- 363 [19] CHEDDADI I., SARAMITO P., DOLLET B., RAUFASTE C.  
364 and GRANER F., *Eur. Phys. J. E*, **34** (2011) 1.
- 365 [20] HASSAGER O., *Nature*, **279** (1979) 402.
- 366 [21] ARIGO M. T. and MCKINLEY G. H., *Rheol. Acta*, **37**  
367 (1998) 307.
- 368 [22] HARLEN O. G., *J. Non Newtonian Fluid Mech.*, **109**  
369 (2002) 411.
- 370 [23] BERIS A. N., TSAMOPOULOS J. A., ARMSTRONG R. C.  
371 and BROWN R. A., *J. Fluid Mech.*, **158** (1985) 219.
- 372 [24] GUYON E., HULIN J. P. and PETIT L., *Hydrodynamique*  
373 *physique* (CNRS Éditions) 2001.
- 374 [25] GRANER F., DOLLET B., RAUFASTE C. and MARMOT-  
375 TANT P., *Eur. Phys. J. E*, **25** (2008) 349.
- 376 [26] DAVIES I. T., COX S. J. and LAMBERT J., *Colloids Surf.*  
377 *A*, **438** (2013) 33.
- 378 [27] REINELT D. A. and KRAYNIK A. M., *J. Fluid Mech.*, **311**  
379 (1996) 327.
- 380 [28] REINELT D. A. and KRAYNIK A. M., *J. Rheol.*, **44** (2000)  
381 453.
- 382 [29] BIANCE A. L., COHEN-ADDAD S. and HÖHLER R., *Soft*  
383 *Matter*, **5** (2009) 4672.
- 384 [30] PRINCEN H. M., *J. Colloid Interface Sci.*, **91** (1983) 160.
- 385 [31] KHAN S. A. and ARMSTRONG R. C., *J. Rheol.*, **33** (1989)  
386 881.
- 387 [32] COX S. J., DOLLET B. and GRANER F., *Rheol. Acta*, **45**  
388 (2006) 403.
- 389 [33] GOYON J., COLIN A., OVARLEZ G., AJDARI A. and BOC-  
390 QUET L., *Nature*, **454** (2008) 84.